THE JOURNAL OF PHYSICAL CHEMISTRY C

Article

pubs.acs.org/JPCC

Phase-Induced Shape Evolution of FeNi Nanoalloys and Their Air Stability by in-Situ Surface Passivation

Nafiseh Moghimi, Samad Bazargan, Debabrata Pradhan,[†] and K. T. Leung*

WATLab and Department of Chemistry, University of Waterloo, Waterloo, Ontario, Canada N2L 3G1

Supporting Information

ABSTRACT: Shape and size of nanoparticles are fundamental structural properties that govern the development of novel surface-related applications. Traditionally external agents such as surfactants, reducing agents, or stabilizers have been used for enforcing preferential growth orientation, size, and shape to develop tailor-made nanoparticles. However, these external agents cover the pristine surface of the particle and invariably reduce the surface activity. Here, we introduce a surfactant-free, single-step electrochemical method to control the shape of air-stable FeNi alloy nanoparticles. Using glancing-incidence X-ray diffraction, we further demonstrate that the shape evolution of nanoparticles from concave cube to truncated sphere occurs concurrently with the phase transformation from bcc to fcc. This shape evolution can be achieved by fine-tuning a single parameter, the ratio of reactant concentrations (i.e., $[Ni^{2+}]/[Fe^{2+}]$). Addition of Ni^{2+} to the Fe^{2+} electrolyte changes the nucleation mechanism from progressive growth for pure Fe^{2+} electrolyte to instantaneous growth for mixed Fe^{2+}/Ni^{2+} electrolyte, which leads to a remarkably narrow size distribution and very uniform dispersion on the Si substrate. Depth-profiling X-ray photoelectron spectroscopy and energy-dispersive X-ray analysis by both transmission electron microscopy and scanning electron microscopy for nanoparticles at different growth stages reveal alloy formation and preferential deposition of Fe during initial growth that results in a quasi-core–shell structure. We also observe the in-situ formation of a very thin Ni-doped FeOOH outer layer and $NiFe_2O_4$ intermediate layer on the skin of the nanoparticles, which passivates the surface and dramatically enhances the air stability. The present work provides a unique example of shape-controlled bimetallic nanostructures and offers insights into growth modification of a host metal structure by a guest metal.

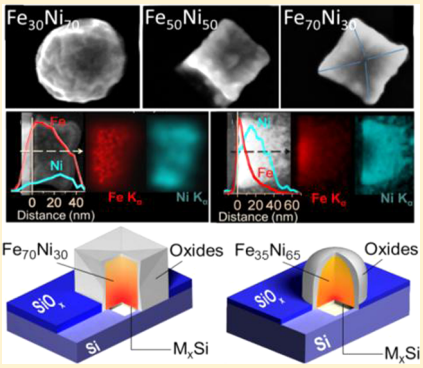

1. INTRODUCTION

Development of bimetallic or trimetallic nanostructured materials, particularly alloy or core–shell nanoparticles (NPs), has attracted much recent attention because of their novel catalytic,[1,2] magnetic,[3−5] and optical properties,[6,7] which could be significantly different from those of their constituent single-metallic materials. The "alloy" properties of these nanoalloys are found to depend not only on their relative compositions and crystal structures but also on their sizes and shapes.[8] Driven by the need for low-cost soft magnets,[9,10] catalysts,[11] and biosensors,[12] the study of bimetallic and trimetallic Fe-based nanoparticles (e.g., FeNi, FeCo, FeCoNi, and FeNiZn) has become a very important research area. As one of the most widely used magnetic materials, FeNi alloys have been synthesized by a variety of methods that usually produce spherical NPs over a large size range (10−500 nm). In wet chemical methods conducted at room temperature, amorphous alloy NPs can be obtained by reverse micelles synthesis and microemulsion process,[13] while crystalline NPs can be produced in various aqueous and nonaqueous media by borohydride reduction and hydrazine reduction of Fe and Ni inorganic salts.[14] However, it is very difficult to obtain a narrow size distribution of NPs with these room-temperature methods, making it necessary to perform the synthesis at a higher temperature (above 300 °C) in the presence of surfactants.[15] Although surfactants could also stabilize the dispersion of NPs and prevent their aggregation, the presence of bulky or strongly binding surfactants around the NPs often affects the properties of the NPs, sometimes in an undesirable way. In dry synthesis methods, such as arc discharge,[16] hydrogen plasma reaction,[17] and reduction of $FeCl_2$ and $NiCl_2$ vapors in the presence of H_2,[18] the spherical NPs or powders so obtained often agglomerate into clusters or chains due to their magnetic interactions. This makes the study and application of uniformly dispersed, individually separated NPs challenging. Besides these difficulties in the synthesis of FeNi alloy nanoparticles with desirable shape, size, and spatial distribution, the easy oxidation of these NPs in air is a serious problem. Air stability is one of the greatest challenges in the synthesis and applications of magnetic metals (Fe-based materials) and it becomes more serious when it comes to the nanoregime because the metallic nanoparticles have a great affinity to oxygen and immediately oxidize in air even at room temperature. Since the magnetic properties change (usually reduce) with oxidation of these

Received: December 16, 2012
Revised: January 27, 2013
Published: February 1, 2013

magnetic nanoparticles, there is a growing interest in developing new ways to keep them stable in air. This further complicates the synthesis methods with the need for an additional surface passivation step including coating with metal oxides[19,20] or encapsulation in polymers,[21] carbon nanotubes,[22] and silica shell.[23] To date, only a few shape-controlled alloy NPs, mostly platinum metal alloys, have been made by using capping reagents, surfactants, diols, or gas reducing agents.[24] Furthermore, despite the large number of studies on the role of alloy component in modifying the structural and other properties of alloy NPs, there is no report on the role of the second metal in the shape evolution of alloy NPs. In the present work, we develop a surfactant-free, single-step, electrochemical deposition (ECD) technique to synthesize air-stable FeNi alloy NPs with different shapes, for the first time, with a narrow size distribution uniformly dispersed on a Si substrate at room temperature. We further demonstrate that the shape evolution of these NPs from Fe-rich concave cube to Ni-rich truncated sphere is correlated with their concurrent phase transformation from bcc (pure Fe phase) to fcc (pure Ni phase). Since the spatial uniformity and size distribution of these NPs deposited on the substrate depend on the type of nucleation (i.e., progressive or instantaneous), we show that the introduction of Ni^{2+} to the Fe^{2+} electrolyte can be used to change the type of nucleation from progressive to instantaneous, resulting in uniform deposition. As a side benefit of the present preparation method, formation of Ni-doped Fe oxides on top of the NPs in situ also passivates the surfaces and results in remarkably air-stable NPs.

2. MATERIALS AND METHODS

FeNi alloy NPs are prepared by ECD on a H-terminated Si(100) substrate in a three-electrode cell workstation (CH Instruments 660A). Silicon chips (15 × 2.5 mm^2, 0.4 mm thick), precut from a Si(100) wafer (p-type, B-doped, with a resistivity of 0.01−0.02 Ω·cm), cleaned using the RCA method, and H-terminated by dipping in an aqueous HF (2%) solution, are used as the working electrode. A standard Ag/AgCl electrode is used as the reference while a Pt wire is used as the counter electrode. The electrolyte consists of different concentrations of Fe^{2+} and Ni^{2+} solutions prepared by dissolving $FeCl_2{\cdot}6H_2O$ and $NiCl_2{\cdot}6H_2O$ salts (Aldrich, 99%) in doubly distilled water, with a 200 mM H_3BO_3 solution used as a supporting electrolyte. In a freshly prepared deoxygenated electrolyte solution, ECD is obtained by amperometry for an appropriate deposition time potentiostatically at −1.4 V vs Ag/AgCl, at which potential Fe^{2+} and Ni^{2+} are reduced to their respective metals. Deposition potential −1.4 V (vsAg/AgCl) is chosen as the optimum potential because −1.2 V results in an inhomogeneous deposition and −1.6 V produces excessive hydrogen evolution. The surface morphology of the NPs so prepared is characterized by field-emission scanning electron microscopy (SEM) in a LEO FE-SEM 1530 microscope. Crystal structures are determined by glancing-incidence X-ray diffraction (GIXRD) in a PANalytical X'Pert Pro MRD diffractometr with Cu Kα (1.542 Å) radiation at an incidence angle of 0.5°. These data are correlated with the local nanostructures and elemental compositions determined by transmission electron microscopy (TEM) in a JEOL 2010F STEM and FEI Tecnai F20 TEM systems, both operating at 200 kV. Chemical-state compositions of the nanoalloys are analyzed as a function of Ar ion sputtering time by depth-profiling X-ray photoelectron spectroscopy (XPS) in a Thermo-VG Scientific ESCALab 250 microprobe with a monochromatic Al Kα radiation (1486.6 eV), operated with a typical energy resolution of 0.4−0.5 full width at half-maximum.

3. RESULTS AND DISCUSSION

Nanoparticles are deposited on a H-terminated Si(100) substrate by amperometry potentiostatically at −1.4 V vs Ag/AgCl in a three-electrode cell. The electrolyte is made up of $FeCl_2$ and $NiCl_2$ solutions of different concentrations, with 200 mM boric acid as the supporting electrolyte. Two series of co-ECD experiments are performed by varying one of the MCl_2 concentrations (M = Fe or Ni) while keeping the other concentration fixed at 5 mM. Figure 1 compares the SEM images of pristine Fe and Ni NPs, prepared by separate ECD in 35 mM of their respective chloride solutions, with those of FeNi alloy NPs prepared by co-ECD for 20 s. Each electrolyte is designated by Fe*X*:Ni*Y*, where *X* and *Y* correspond to the concentrations (in mM) of $FeCl_2$ and $NiCl_2$ solutions, respectively. The corresponding Ni at. % and the respective Ni mole fraction of the electrolyte are summarized in Table 1. For ECD in Fe35, cubic Fe NPs are observed together with bigger NP clusters with a broad size distribution, which suggests progressive nucleation in the growth mechanism of these Fe NPs. By introducing Ni^{2+} as a second component into the Fe^{2+} solution, the average size of the cubic NPs in the Fe30:Ni5 solution becomes larger but with reduced clustering (Figure 1, left column; Table 1). This shows that the nucleation has changed from a progressive to instantaneous mechanism (Supporting Information, Figure S1), which results in uniform deposition and a narrow size distribution. By keeping the $NiCl_2$ concentration constant at 5 mM while reducing the $FeCl_2$ concentration, the average size of the cubic NPs has decreased with the corresponding size distribution becoming notably

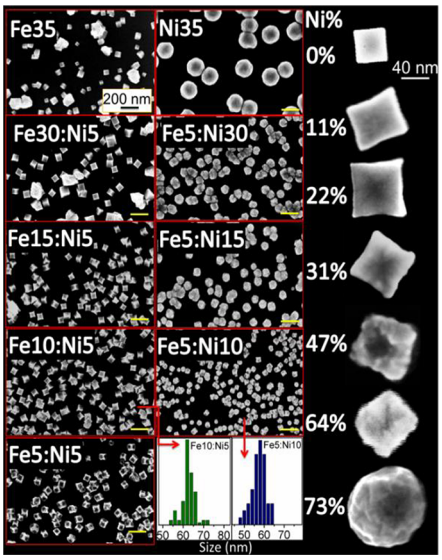

Figure 1. SEM images of FeNi alloy nanoparticles electrodeposited on a H−Si(100) substrate at −1.4 V (vs Ag/AgCl) for 20 s in different Fe*X*:Ni*Y* solutions, where *X* and *Y* correspond to the concentrations in mM of $FeCl_2$ and $NiCl_2$, respectively. Center bottom panel presents the corresponding particle size distributions for Fe10:Ni5 and Fe5:Ni10. Right panel shows the high-magnification SEM images of FeNi alloy NPs for Ni at. % (as determined by EDX) of 0% (Fe35), 11% (Fe30:Ni5), 22% (Fe15:Ni5), 31% (Fe10:Ni5), 47% (Fe5:Ni5), 64% (Fe5:Ni10), and 73% (Fe5:Ni15).

dx.doi.org/10.1021/jp312391h | J. Phys. Chem. C 2013, 117, 4852−4858

Table 1. Atomic Percentage of Ni Obtained by EDX, Average Size, Phase Combination and Lattice Constants Deduced by XRD for FeNi Alloy NPs Obtained from Fe*X*:Ni*Y* Electrolytes (with the Corresponding Ni Mole Fraction)[a]

Fe*X*:Ni*Y* (*X*, *Y* in mM)	Ni mole fraction (%) in electrolyte	Ni content (at. %) obtained by EDX	average size (nm)	phase[b]	lattice constant (Å)
Fe35	0	0	56 with clusters	bcc	2.864
Fe30:Ni5	14	11	78 ± 8	bcc	2.866
Fe15:Ni5	25	22	70 ± 5	76% bcc + 24% fcc	2.867, 3.583
Fe10:Ni5	33	31	63 ± 3	61% bcc + 39% fcc	2.867, 3.587
Fe5:Ni5	50	47	62 ± 2	43% bcc + 57% fcc	2.866, 3.572
Fe5:Ni10	67	64	58 ± 2	fcc	3.544
Fe5:Ni15	75	73	93 ± 5	fcc	3.539
Fe5:Ni30	86	81	100 ± 6	fcc	3.529
Ni35	100	100	163 ± 7	fcc	3.525

[a]Pure Fe (Fe35) and Ni (Ni35) nanoparticles are included as references. [b]For nanoalloy with a mixture of two phases, the relative amounts for bcc and fcc phases are obtained by using a nonlinear least-squares optimization peak-fitting software.

narrower. On the other hand, ECD in Ni35 produces more uniform deposition of considerably larger spherical NPs and a narrower size distribution, which suggests an instantaneous growth mechanism. By introducing Fe^{2+} as a second component into the Ni^{2+} solution, the average size of the spherical NPs becomes notably smaller (Figure 1, center column; Table 1). As the electrolyte becomes Ni-rich, the morphology changes to truncated sphere. The distorted nanospheres become more and more faceted, along with emergence of some truncated cubes, truncated octahedron, and other distorted cubes, as the Ni^{2+} concentration approaches the Fe^{2+} concentration. The corresponding size distribution plots for NPs obtained from Fe10:Ni5 and Fe5:Ni10 solutions are shown in Figure 1. The size distribution of the concave cubic samples (e.g., Fe10:Ni5) is found to be narrower than that of the truncated spherical samples (e.g., Fe5:Ni10) (Figure 1, bottom center), which is likely due to the well-defined shape of the nanocubes.

The high-magnification SEM images, shown in Figure 1 (right panel), illustrate the shape evolution of FeNi nanoalloys with increasing Ni content. When the concentration of Fe^{2+} is more than that of Ni^{2+} in the electrolyte, the dominant shape follows the cubic shape of the pristine Fe NP. Adding Ni atoms into the Fe host system changes the regular cubic shape to concave cubic, which is more obvious at 31 at. % Ni (Fe10:Ni5). As the relative Ni^{2+} electrolyte concentration increases, the edges of the nanocubes appear to have an increasing concave curvature, giving rise to pointy corners without introducing new spherical shape characteristic of the Ni NPs. For the electrolyte with equal Fe^{2+} and Ni^{2+} concentrations (Fe5:Ni5), an indentation at the center of a cubic face is clearly observed (Figure 1, right column). As the electrolyte becomes Ni-rich, the morphology changes to truncated spherical, following the spherical morphology of the pristine Ni NP, and the presence of Fe introduces facets into the spherical shape.

Although phase transformation from bcc to fcc as a function of Ni atomic content has been observed in FeNi bulk alloys[25,26] and ultrafine FeNi particles,[17,18] the connection between this phase transformation and the shape of NPs remains unclear. We investigate the shape evolution of FeNi alloy NPs from concave cubic to truncated spherical with increasing Ni atomic content by glancing-incidence XRD for FeNi alloy NPs obtained by co-ECD in different electrolytes. No diffraction patterns of pure metallic Fe or Ni (and their oxides) are observed, which indicates the absence of segregated metal NPs. The region of 2θ = 50°−60° contains mainly diffraction features of the Si(100) substrate and is therefore not shown (Figure 2). For NPs obtained with the Fe30:Ni5 electrolyte, the

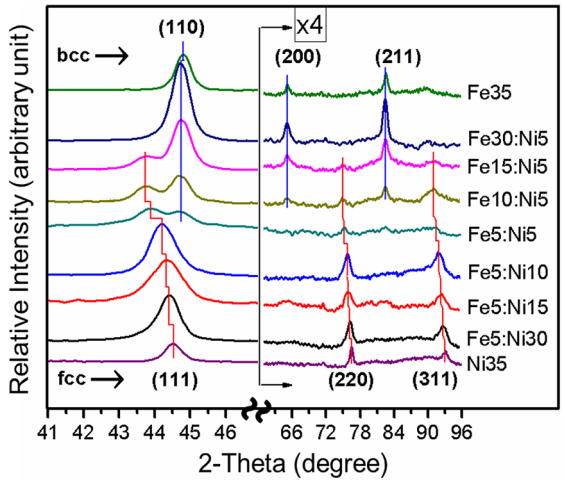

Figure 2. Glancing-incidence XRD patterns of FeNi alloy nanoparticles electrodeposited on a H−Si(100) substrate at −1.4 V (vs Ag/AgCl) for 20 s in different Fe*X*:Ni*Y* solutions, where *X* and *Y* correspond to the concentrations of $FeCl_2$ and $NiCl_2$ in mM, respectively.

most intense diffraction peak, (110), is shifted to a lower 2θ value, indicating lattice expansion as a result of alloy formation in the bcc phase region of the FeNi alloy phase diagram.[27] Increasing the relative Ni content to 22 at. % with Fe15:Ni5 (Table 1) introduces a new set of features corresponding to the fcc phase of the FeNi alloy. With further increase in the relative Ni content to 31 at. % (Fe10:Ni5) and 47 at. % (Fe5:Ni5), the diffraction features for the fcc alloy phase are found to shift to a higher 2θ value, which indicates lattice contraction due to the gradual inclusion of the smaller "guest" Ni atoms into the lattice of the larger "host" Fe atoms. The increase in the relative Ni content also appears to reduce the intensities of the bcc diffraction peaks without affecting their 2θ locations (Figure 2). For NPs obtained with the Fe5:Ni5 electrolyte, the fcc alloy phase becomes more dominant than the bcc alloy phase, with the (111) feature of the fcc phase becoming the most prominent while the diffraction features for the bcc phase greatly diminished in intensity. Further increase in the Ni content from 47 at. % (Fe5:Ni5) to 64 at. % (Fe5:Ni10), 73 at. % (Fe5:Ni15), and 81 at. % (Fe5:Ni30) (Table 1) produces a

dx.doi.org/10.1021/jp312391h | J. Phys. Chem. C 2013, 117, 4852−4858

single set of diffraction features corresponding to the fcc phase of FeNi alloy. These features are also found to be shifting toward a higher 2θ, converging to the diffraction pattern of the Ni fcc phase (Ni35). Concave cubic structures are formed when the fcc unit cells are introduced as the guest to the main bcc host phase (from Fe15:Ni5 to Fe5:Ni5). When the phase transition from bcc to fcc is complete (Fe5:Ni10), the final shape of NPs is found to switch from concave cubic to truncated spherical. Of particular interest is that the concave cubic shape becomes most obvious (Figure 1, right panel), when the relative concentrations of Fe and Ni are the same in the electrolyte (Fe5:Ni5) and the amounts of bcc and fcc phases are almost equal (Table 1, Figure 2). The deep indentations in the concave faces of NPs obtained from Fe5:Ni5 have become filled in, converting the NPs to more spherical, as the Ni content increases into the Ni-rich regime (Figure 1, right panel). XRD patterns of the NPs obtained in different stages of the growth (i.e., with different deposition times) from Fe5:Ni5 show the initial formation of bcc phase and the subsequent growth of the fcc unit cells in the bcc host lattice (Supporting Information, Figure S2), which lead to the concave cubic shape similar to that found for the Fe-rich alloy NPs. It therefore confirms that even when both phases are present in equal amounts, the final shape of NPs is governed by the Fe host crystal structure.

To confirm alloy formation and the absence of segregated Fe or Ni NPs or domains inside the NPs, we collect XPS spectra of Fe 2p and Ni 2p regions as a function of sputtering depth. To identify the peak locations and the corresponding chemical shifts, we have fitted the spectra with Gaussian−Lorentzian line shapes using the CasaXPS program, after appropriate correction with the Shirley background. To remove the carbonaceous layer commonly found due to sample handling in air, we perform Ar sputtering of the as-prepared samples for 10 s. The resulting chemical-state compositions for typical FeNi alloy concave nanocubes and truncated nanospheres are compared with those for pure Fe and Ni NPs in Figure 3 (also after 10 s of sputtering), respectively. Compared to the pristine Ni NPs, the Ni $2p_{3/2}$ peaks at 852.9 eV has a discernible shift of 0.3 eV toward higher binding energies for alloy nanocubes, while no obvious differences in the Fe $2p_{3/2}$ peak position from the pristine Fe NPs is observed (Figure 3a,b). On the other hand, for the FeNi nanospheres, the metallic Fe $2p_{3/2}$ peak exhibits a 0.3 eV binding energy shift to a higher binding energy and the Ni $2p_{3/2}$ peak location does not change (Figure 3e,f). The peaks at 855.6 and 709.6 eV are related to the Ni and Fe oxides, respectively, in a thin oxide shell of the alloy NP, which are removed completely after 190 s sputtering. Continued sputtering to 1030 s for both nanocubes and nanospheres reduces the metallic Fe and Ni features, with the emergence of a new Fe $2p_{3/2}$ feature at 707.2 eV and a new Ni $2p_{3/2}$ feature at 853.6 eV attributable to Fe silicide and Ni silicide, respectively.[28,29] It should be noted that the Si 2p peak remains unchanged at 99.4 eV because of the overwhelming contribution from bulk silicon (not shown). The broad peak at 712.2 eV found after 70 s of sputtering and remained up to 1390 s of sputtering in FeNi nanospheres (Figure 3f) corresponds to the Ni $L_3M_{23}M_{45}$ Auger transition.[28] The presence of detectable Ni Auger feature for the FeNi nanospheres and not the FeNi nanocubes confirms the higher Ni content in the former.

According to the charge transfer theory for transition metal alloys,[30] we calculate the partial charge transfers, ΔZ_A, for Fe

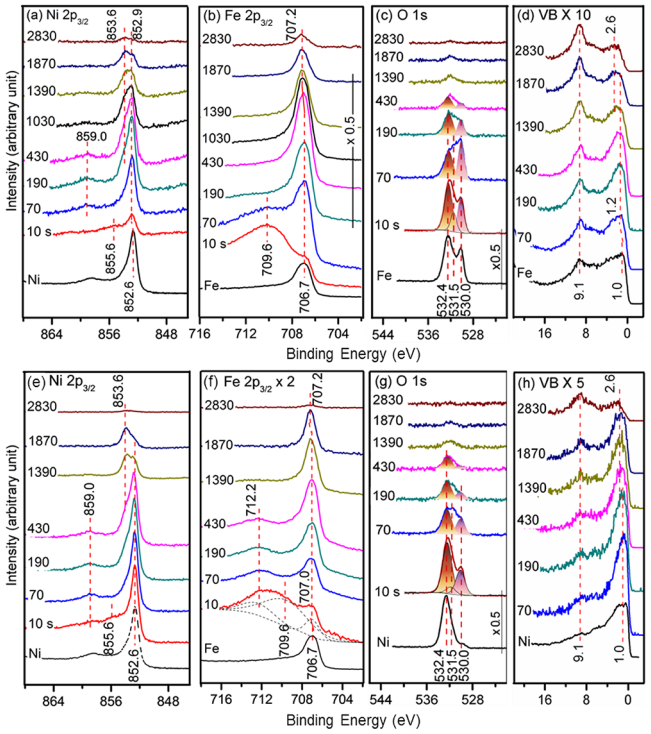

Figure 3. XPS spectra of (a, e) Ni 2p, (b, f) Fe 2p, (c, g) O 1s, and (d, h) valence band (VB) regions for FeNi alloy nanocubes as-electrodeposited on H−Si(100) in Fe10:Ni5 (upper panels) and nanospheres obtained in Fe5:Ni10 electrolyte (lower panels) and upon sputtering for 10, 70, 190, 430, 1390, 1870, and 2830 s. The corresponding Ni 2p (a, e) and VB spectra (h) for pristine Ni nanoparticles obtained in Ni35 and Fe 2p (b, f) and VB spectra (d) for pristine Fe nanoparticles obtained in Fe35 are also shown for comparison.

(Ni) to be 0.17 (0.34) per atom in the nanocubes and 0.34 (0.17) per atom in the nanospheres using the relation

$$\Delta Z_A = 1.2(1 - C_A)\Delta\varphi^*$$

where $\Delta\varphi^*$ is the difference in electronegativities of the metals and C_A is the concentration of metal A. The smaller partial charge transfers for Fe 2p (Ni 2p) in Fe-rich (Ni-rich) alloy NPs also explain the lack of discernible binding energy shift in XPS spectra. The lack of a discernible binding energy shift for Fe in the nanocubes and for Ni in the nanospheres could be due to the weak electron transfer and/or to the strong photopeak from the majority metal in the nanocubes (Fe) and nanospheres (Ni), respectively, that overwhelms any weak feature corresponding to the alloy peak.

The O 1s feature at 530.0 eV (Figure 3c) corresponds to O^{2-} species, which includes very close-lying FeO, NiO, and/or $NiFe_2O_4$ features.[31,32] Similarly, the feature at 531.5 eV corresponds to OH^-, which is due to contributions of $Ni(OH)_2$ and/or FeOOH.[31,33] The remaining O 1s feature at 532.4 eV can be assigned primarily to SiO_x from the bare substrate region not covered by NPs. The O 1s features are reduced dramatically (by over 60%) upon just 70 s of sputtering and more gradually upon further sputtering, which confirms the removal of the thin oxide skin on the nanocubes and subsequent SiO_x removal on the rest of the substrate. In particular, the O 1s feature at 531.5 eV is found to be removed first, and this is followed by the depletion of feature at 530.0 eV.

dx.doi.org/10.1021/jp312391h | J. Phys. Chem. C 2013, 117, 4852−4858

This implies the possibility of two oxide region with different composition.

In the valence band spectra for the as-deposited FeNi concave nanocubes (Figure 3d) and truncated nanospheres (Figure 3h), the electron density of states is found to be broadly distributed between 0 and 4 eV, with significant intensity at the Fermi level characteristic of a metal. The valence band maximum for FeNi nanocubes (Figure 3d) located at 1.2 eV is 0.2 eV higher than that for pristine Fe NPs (Figure 3d, bottom trace), which is in good accord with the spectrum of invar FeNi alloy.[34] The valence band spectra of the FeNi nanospheres (Figure 3h) exhibit a sharper density of states distribution than nanocubes (Figure 3d) and more closely resemble that of the pristine Ni NPs (Figure 3h, bottom trace). There is no discernible shift for the valence band maximum for the as-deposited nanospheres and upon sputtering for 430 s. Sputtering nanocubes and nanospheres for 1390 s exposes the feature at 2.6 eV, which can be attributed to the hybridized Fe 3d−Si 2p or Ni 3d−Si 3p states,[35] similar to the M−Si 3s features (M = Ni, Co) reported by Tersoff.[36] The strong peak at 9.1 eV that becomes more intense with increasing sputtering time corresponds to Ar 3p feature of implanted Ar as a result of sputtering.

Figures 4a and 4b show the corresponding depth profiles for Fe $2p_{3/2}$ peaks for the alloy at 706.7 and 707.0 eV and Fe-silicide at 707.2 eV, the Ni $2p_{3/2}$ peaks for the alloy at 852.6 and 852.9 eV and Ni-silicide at 853.6 eV, and the O 1s peaks for all oxides at 530.0 and 531.5 eV for the nanocubes and nanospheres, respectively. For nanocubes (Figure 4a), the metal silicide features begin to emerge upon sputtering for ∼1000 s, which marks the interface between the NP and the Si substrate. On the other hand, the metal oxide features are found to be removed rapidly after brief initial sputtering for 70 s and completely removed after 430 s of sputtering, indicating a thin oxide shell. In between the oxide shell and the NP−Si interface, we identify the alloy core region, in which the Fe alloy profile is higher than the Ni alloy profile due to the higher Fe content in the Fe10:Ni5 electrolyte. More importantly, the relative intensities of the Fe and Ni alloy features are found to be changing gradually inside this alloy core region, which suggests the presence of a Fe relative composition gradient increasing toward the interface. For the nanospheres (Figure 4b), the Ni silicide feature emerges after 900 s of sputtering while the weaker Fe silicide feature occurs after ∼1800 s. The oxide features are found to be totally removed after just 190 s of sputtering. These trends indicate the presence of a similar metal silicide region and a metal oxide shell region. Furthermore, a metal alloy core region is also observed, with the Ni alloy profile lying higher than the Fe alloy profile due to the higher Ni content resulting from deposition in the Fe5:Ni10 electrolyte. Interestingly, the weaker Fe alloy profile is found to cross over the stronger Ni alloy profile at ∼1000 s of sputtering. Despite the Ni-rich composition of the alloy nanospheres, the gradual change in the relative composition of Fe in the alloy core region leads to a higher Fe alloy composition at the NP−Si interface. This suggests a faster Fe nucleation than Ni nucleation, leading to a Fe-rich nucleus, during the initial stage of alloy NP formation.

TEM-EDX line scans across a typical nanocube (Figure 4c) and a nanosphere (Figure 4d) also confirm the corresponding XPS depth profiles shown in Figures 4a and 4b. The similarity between the XPS depth profile and the corresponding TEM-EDX profile shows that both the nanocubes (Figure 4a,c) and

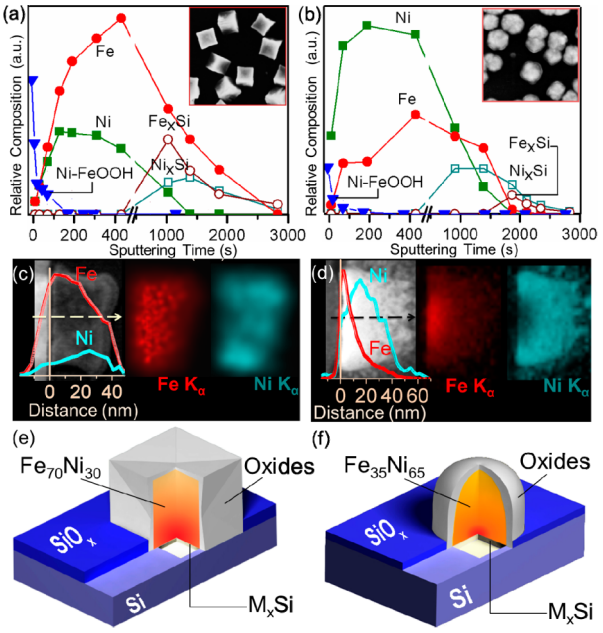

Figure 4. Depth profiles of Fe $2p_{3/2}$ features for alloy at 706.7 and 707.0 eV and Fe silicides at 707.2 eV and Ni $2p_{3/2}$ features for alloy at 852.6 and 852.9 eV and Ni silicides at 853.6 eV for (a) FeNi alloy concave nanocubes obtained from a Fe10:Ni5 electrolyte and (b) FeNi alloy truncated nanospheres obtained from a Fe5:Ni10 electrolyte. (c) and (d) show EDX line scans and EDX-TEM cross-sectional mapping of a typical concave nanocube and nanosphere. Schematic models of (e) a FeNi nanocube and (f) a FeNi nanosphere as inferred from depth-profiling XPS and TEM data. Both FeNi alloy cores are also covered by an oxide shell (consisting of Ni-doped FeOOH and $NiFe_2O_4$) supported on the Si substrate with a metal silicide (M_xSi) interface.

nanospheres (Figure 4b,d) are highly homogeneous in composition. From both XPS depth profiling and TEM-EDX line scans, it can be observed that despite the difference in shape, both nanocubes and nanospheres exhibit an alloy−core oxide−shell structure. Depending on the electrolyte composition, the alloy core can be either Fe-rich or Ni-rich at the core region with a gradual composition change extending into the Fe-rich nucleus. From the O 1s depth profile, we estimate the thickness of the oxide shell to be 5.3 nm, using the sputtering rate of 0.74 nm/min obtained for this sample determined by profilometry. This thickness is found to be in good agreement with the thickness (∼6 nm) obtained from a line scan of the corresponding TEM-EDX data (not shown). Schematic diagrams illustrating the respective compositions of the FeNi alloy nanocube and nanosphere are presented in Figures 4e and 4f.

To investigate the nature of the oxide shell, we show in Figure 5a the Fe $2p_{3/2}$ and Ni $2p_{3/2}$ spectra for the FeNi concave nanocubes as-prepared from a Fe10:Ni5 electrolyte and upon Ar^+ sputtering for 10 and 40 s. The Fe $2p_{3/2}$ peak at 710.3 eV can be attributed to FeOOH, in accord with the 710.7 eV position found in our reference sample (not shown) and the literature.[31] The small difference could be due to Ni incorporation in the oxide shell and is consistent with the Ni $2p_{3/2}$ oxide peak at 855.6 eV. As the electrolytes consist of $FeCl_2$ and $NiCl_2$, and given the formation of β-FeOOH in the chloride solution,[37] Ni^{2+} could be doped into the β-FeOOH structure in the presence of Cl^-.[38] After sputtering for 40 s, the Fe $2p_{3/2}$ peak (at 710.3 eV) is found to shift to a lower binding

dx.doi.org/10.1021/jp312391h | J. Phys. Chem. C 2013, 117, 4852−4858

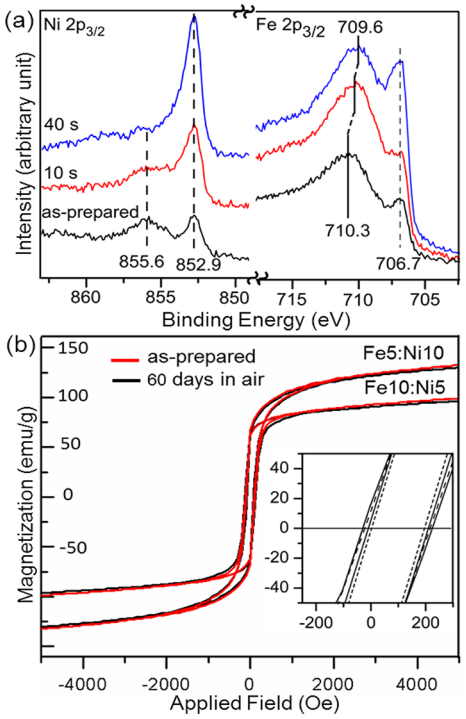

Figure 5. (a) Fe $2p_{3/2}$ and Ni $2p_{3/2}$ spectra for the as-prepared nanoparticles from Fe10:Ni5 electrolyte and sputtered by Ar^+ for 10 and 40 s. (b) Magnetization hysteresis loops measured at room temperature and coercivity (inset) for samples as-prepared from Fe10:Ni5 and Fe5:Ni10 electrolytes (solid lines) and upon exposure to the humid air (80% relative humidity) for 60 days (dashed line).

energy with appearance of a small shoulder, revealing the presence of an intermediate oxide layer attributable to $NiFe_2O_4$.[39] Formation of an intermediate $NiFe_2O_4$ layer has also been observed in the steel alloys.[40] The oxide shell therefore consists of Ni-doped FeOOH in the outer shell and $NiFe_2O_4$ in the inner shell. The growth mechanism of the oxide shell is given in the Supporting Information.

One of the great challenges in synthesis of magnetic materials, such as Fe, Ni, and Co and their alloys, particularly in the nanoscale, is their very high air activity and easy oxidization. To protect the metallic nanoparticles from oxidation, an additional step of coating the NP with transition-metal oxides[19,20] or encapsulation in polymers,[21] carbon nanotubes,[22] and silica shell[23] is often required. In the present work, the oxide layer formed in situ on the FeNi NPs in the co-ECD eliminates such an extra step. From their corresponding TEM-EDX line scans and XPS depth-profile data, we estimate this oxide layer to be 6 nm thick for concave nanocubes and ~5 nm thick for truncated nanospheres, with the majority of the NPs (~95 vol %) remaining as metallic. To evaluate the resistance of these NPs to oxidation in air, the samples were placed in an air environment with 80% relative humidity at room temperature for 60 days. No diffraction peak attributable to oxides in XRD and less than 5% increase in the amount of oxygen in EDX are observed for both NPs. More precisely, the change in magnetization saturation and coercivity of nanoparticles can show the change in the amount of the metallic part and changes in the nature of the material. We have used this technique to investigate if any further oxidation occurs after keeping the nanoparticles in air for a long time. The magnetization saturation obtained from SQUID hysteresis loops is found to decrease only by just 0.8% in the concave nanocubes and 1.2% in the truncated nanospheres, which are within the experimental uncertainty of the measurement. Therefore, there is effectively no change in the magnetization saturation. Similarly, almost no change in coercivity of both concave nanocubes and truncated nanospheres is observed. These data demonstrate that effectively no metallic part of NPs has been converted to oxide. All of these data therefore support the remarkable air stability of these NPs (Figure 5b). The presence of Ni-incorporated FeOOH, along with the denser intermediate layer of $NiFe_2O_4$, on the NPs inhibits corrosion of NPs in air, which is in good agreement with the anticorrosive properties of Ni-doped FeOOH and of the $NiFe_2O_4$ protective layer in steel alloys.[38,40]

4. CONCLUSION

In the present work, near-monosized FeNi alloy NPs are obtained by a single-step co-electrodeposition method with a good control on shape, structure, and composition. By changing the Fe:Ni ratio, we can obtain different compositions and different shapes from concave cubic Fe-rich alloy NPs to truncated spherical Ni-rich alloy NPs. In the initial growth stage, FeNi alloy NPs follow instantaneous nucleation, in contrast to pristine Fe NPs that follow the progressive nucleation. This leads to a very narrow size distribution and prevents clustering in the NPs growth. We study the effect of addition of a second metal to a host metal lattice on changing the final shape of the resulting bimetallic NP system and demonstrate the important role of phase transformation in the shape evolution of FeNi NPs from concave cubic to truncated spherical shape. XPS depth profiling and elemental TEM-EDX line scan show Fe-rich nucleus for both nanocubes and nanospheres and a composition gradient inside the NPs where Fe content is gradually decreasing from the Si interface toward the oxide surface that modifies the surface function. Depending on the electrolyte composition, the alloy NP can be either Fe-rich or Ni-rich in the core region. A thin protective oxide layer consisting of a Ni-doped FeOOH outer layer and $NiFe_2O_4$ intermediate layer can be obtained in situ over the entire metallic core, which provides effective corrosion protection. We have successfully extended our present co-electrodeposition method as a general approach to synthesize other nanoalloy materials, including concave cubic FeCo, tetragonal and hexagonal FeZn, and truncated spherical NiCo NPs. This study provides new insight into the use of guest metal in a host system as a parameter to control the shape of bimetallic or alloy nanoparticles.

■ ASSOCIATED CONTENT

Ⓢ Supporting Information

Nucleation mechanism and mechanism of oxide shell formation. This material is available free of charge via the Internet at http://pubs.acs.org.

■ AUTHOR INFORMATION

Corresponding Author

*E-mail: tong@uwaterloo.ca.

Present Address

†Materials Science Center, Indian Institute of Technology, Kharagpur, India.

Notes

The authors declare no competing financial interest.

■ ACKNOWLEDGMENTS

This work was supported by the Natural Sciences and Engineering Research Council of Canada.

■ REFERENCES

(1) Soriaga, M. P. *Chem. Rev.* **1990**, *90*, 771−793.
(2) Yim, W.-L.; Klüner, T. *J. Phys. Chem. C* **2010**, *114*, 7141−7152.
(3) Polshettiwar, V.; Luque, R.; Fihri, A.; Zhu, H.; Bouhrara, M.; Basset, J.-M. *Chem. Rev.* **2011**, *111*, 3036−75.
(4) Derosa, P. A.; Seminario, J. M.; Balbuena, P. B. *J. Phys. Chem. A* **2001**, *105*, 7917−7925.
(5) Li, G.-R.; Zhang, Z.-S.; Su, C.-Y.; Tong, Y.-X. *J. Phys. Chem. C* **2009**, *113*, 1227−1234.
(6) Ferrando, R.; Jellinek, J.; Johnston, R. L. *Chem. Rev.* **2008**, *108*, 845−910.
(7) Cortie, M. B.; McDonagh, A. M. *Chem. Rev.* **2011**, *111*, 3713−35.
(8) Teng, X.; Yang, H. *Front. Chem. Eng. China* **2010**, *4*, 45−51.
(9) Vitta, S.; Khuntia, A.; Ravikumar, G.; Bahadur, D. *J. Magn. Magn. Mater.* **2008**, *320*, 182−189.
(10) Rao, B.; Ramos de Debiaggi, S.; Jena, P. *Phys. Rev. B* **2001**, *64*, 1−6.
(11) Shen, W.; Huggins, F. E.; Shah, N.; Jacobs, G.; Wang, Y.; Shi, X.; Huffman, G. P. *Appl. Catal., A* **2008**, *351*, 102−110.
(12) Behrens, S.; Bönnemann, H.; Matoussevitch, N.; Gorschinski, A.; Dinjus, E.; Habicht, W.; Bolle, J.; Zinoveva, S.; Palina, N.; Hormes, J.; Modrow, H.; Bahr, S.; Kempter, V. *J. Phys.: Condens. Matter* **2006**, *18*, S2543−S2561.
(13) Ban, I.; Drofenik, M.; Makovec, D. *J. Magn. Magn. Mater.* **2006**, *307*, 250−256.
(14) Wang, H.; Li, J.; Kou, X.; Zhang, L. *J. Cryst. Growth* **2008**, *310*, 3072−3076.
(15) Chen, Y.; She, H.; Luo, X.; Yue, G.-H.; Mi, W.-B.; Bai, H.-L.; Peng, D.-L. *J. Nanosci. Nanotechnol.* **2010**, *10*, 3053−3059.
(16) Lu, B.; Huang, H.; Dong, X. L.; Zhang, X. F.; Lei, J. P.; Sun, J. P.; Dong, C. *J. Appl. Phys.* **2008**, *104*, 114313.
(17) Dong, X. L.; Zhang, Z. D. *J. Mater. Res.* **1999**, *109*, 7203−7.
(18) Suh, Y.; Jang, H.; Chang, H.; Kim, W.; Kim, H. *Powder Technol.* **2006**, *161*, 196−201.
(19) Wang, C. M.; Baer, D. R.; Amonette, J. E.; Engelhard, M. H.; Qiang, Y.; Antony, J. *Nanotechnology* **2007**, *18*, 255603.
(20) Shavel, A.; Rodríguez-González, B.; Spasova, M.; Farle, M.; Liz-Marzán, L. M. *Adv. Funct. Mater.* **2007**, *0*, 1−7.
(21) Ponder, S. M.; Darab, J. G.; Bucher, J.; Caulder, D.; Craig, I.; Davis, L.; Edelstein, N.; Lukens, W.; Nitsche, H.; Rao, L.; Shuh, D. K.; Mallouk, T. E. *Chem. Mater.* **2001**, *13*, 479−486.
(22) Xu, M. H.; Zhong, W.; Qi, X. S.; Au, C. T.; Deng, Y.; Du, Y. W. *J. Alloys Compd.* **2010**, *495*, 200−204.
(23) Ammar, M.; Mazaleyrat, F.; Bonnet, J. P.; Audebert, P.; Brosseau, A.; Wang, G.; Champion, Y. *Nanotechnology* **2007**, *18*, 285606.
(24) Wu, J.; Gross, A.; Yang, H. *Nano Lett.* **2011**, *11*, 798−802.
(25) Zhu, L. H.; Ma, X. M.; Zhao, L. *J. Mater. Sci.* **2001**, *36*, 5571−5574.
(26) Valderruten, J. F.; Pérez Alcázar, G. A.; Grenèche, J. M. *J. Phys.: Condens. Matter* **2008**, *20*, 485204.
(27) Bradley, A. J.; Jay, A. H.; Taylor, A. *Philos. Mag.* **1973**, *23*, 155.
(28) Moulder, J. F.; Stickle, W. F.; Sobol, P. E.; Bomben, K. D. In *Handbook of X-ray Photoelectron Spectroscopy*, 2nd ed.; Chastain, J., Ed.; Perkin-Elmer Corp.: Eden Prairie, MN, 1992.
(29) Rührnschopf, K.; Borgmann, D.; Wedler, G. *Thin Solid Films* **1996**, *280*, 171−177.
(30) Miedema, A. R. *J. Less-Common Met.* **1973**, *32*, 117−136.
(31) Suzuki, S.; Yanagihara, K.; Hirokawa, K. *Surf. Interface Anal.* **2000**, *30*, 372−376.
(32) Li, X.; Zhang, W. *Society* **2006**, 4638−4642.
(33) Matlosz, M. *J. Electrochem. Soc.* **1993**, *140*, 2272.
(34) Zakharov, A. I.; Narmonev, A. G.; Batirev, I. G. *J. Magn. Magn. Mater.* **1984**, *44*, 105−108.
(35) Kinsinger, V.; Dezsi, I.; Steiner, P.; Langouche, G. *J. Phys.: Condens. Matter* **1990**, *2*, 4955.
(36) Tersoff, J.; Hamann, D. R. *Phys. Rev. B* **1983**, *28*, 1168−1170.
(37) Mohapatra, M.; Mohapatra, L.; Anand, S.; Mishra, B. K. *J. Chem. Eng. Data* **2010**, *55*, 1486−1491.
(38) Chung, K. W.; Kho, Y. T.; Kim, K. B. *Corros. Sci.* **2002**, *44*, 2757−2775.
(39) Nawale, A. B.; Kanhe, N. S.; Patil, K. R.; Bhoraskar, S. V.; Mathe, V. L.; Das, A. K. *J. Alloys Compd.* **2011**, *509*, 4404−4413.
(40) Nishimura, T.; Katayama, H.; Noda, K. *Corros. Sci.* **2000**, *42*, 1611−1621.